Direct Observation of the Kinetics of Gas-Solid Reactions using In-situ Kinetic and Spectroscopic Techniques

Journal:	*Reaction Chemistry & Engineering*
Manuscript ID	RE-ART-02-2018-000020.R1
Article Type:	Paper
Date Submitted by the Author:	20-Apr-2018
Complete List of Authors:	Hoffman, Adam; Stanford Linear Accelerator Center Azzam, Sara; University of California at Los Angeles, Department of Chemical and Biomolecular Engineering Zhang, Kai; Institute of High Energy Physics, Xu, Yahong; Stanford Synchrotron Radiation Lightsource Liu, Yijin; Stanford Synchrotron Radiation Lightsource, Bare, Simon; Stanford Linear Accelerator Center Simonetti, Dante; University of California at Los Angeles, Department of Chemical and Biomolecular Engineering

Journal Name

ARTICLE

Direct Observation of the Kinetics of Gas-Solid Reactions using *In-situ* Kinetic and Spectroscopic Techniques

Received 00th January 20xx,
Accepted 00th January 20xx

DOI: 10.1039/x0xx00000x

www.rsc.org/

Adam S. Hoffman[b,†], Sara Azzam[a,†], Kai Zhang[b,c,†], Yahong Xu[b], Yijin Liu[b,*], Simon R. Bare[b,*],

Dante A. Simonetti[a,*]

Developing fundamental insight for reactions between gas phase H_2S and solid phase CuO has the potential to lead to improved materials and processes for natural gas purification. However, this insight requires detailed knowledge of the atomistic characteristics of the solid and how these characteristics influence the reaction mechanism and kinetics. Herein, we use fixed bed reactors, X-ray absorption spectroscopy, and transmission X-ray microscopy to simultaneously probe the fundamental kinetics of the reaction of CuO with H_2S to form CuS, and thereby probe spatial-temporal chemical and structural changes of copper during this reaction. H_2S removal reaction kinetics show similar trends in fixed bed reactors as in 10-20 μm sized particles. However, reaction fronts proceed through the entire diameter of particles heterogeneously, indicating the presence of pore diffusion resistance even at very small length scales. In addition, CuO sorbent samples with similar characteristics exhibit 3 times different sulfidation conversion with reaction rate constants that differ by a factor of 1.5. These differences in reaction kinetics and conversion indicate the critical impact of possible atomic scale differences and the formation of different copper sulfide products.

Introduction

As the global energy portfolio becomes increasingly decarburized over the next decades, abundant natural gas will serve as a critical transitional energy resource. Indeed, much research has already been conducted to utilize natural gas in energy and chemical synthesis applications[1]. However, natural gas streams typically contain a wide range of contaminants and require purification before processing because these contaminants damage process equipment and catalysts and are hazardous to humans and the environment[2,3]. Adsorptive separation processes are a practical way to remove trace amounts (1-100 ppm-mol) of sulfur compounds (e.g., mercaptans, H_2S, CS_2, COS)[2,3] that exist as contaminants in these streams. Many regenerable adsorbents can remove these contaminants. However, reaction of these species with a solid phase (known as reactive sorption) is advantageous because (i) the thermodynamics are more favorable compared to adsorption, leading to higher purity streams and higher solid phase contaminant capacities and (ii) the contaminants are permanently sequestered in a stable and environmentally benign form (e.g., as a metal sulfide)[4-7]. The primary drawbacks with current reactive sorption materials are incomplete conversion and mass-transfer limited rates[6-9]. These limitations can result from either morphology (e.g., decreasing porosity) and/or chemical structure changes (i.e., changes at the product-reactant interface) that occur during reaction[10,11].

Indeed, the technologies that remove sulfur contaminants from natural gas need to be very well understood so that existing and future gas conversion technologies can be deployed successfully. Developing fundamental insight for these gas-solid reactions requires characterization at the molecular/atomistic level while also collecting reaction kinetic data to use in microkinetic models that enable reaction model parameters to be related to chemical and structural changes[12]. These fundamental models have parameters with distinct physical meanings and can be used across a wide range of conditions and materials. Only a few recent studies have used both advanced characterization and kinetic studies to develop such molecular descriptions of gas-solid reaction systems[6,7,13,14], and very few previous studies have attempted to probe, in real time, the spatial and chemical conversion of solid phases during reaction with gaseous species[6,7].

[a] *Chemical and Biomolecular Engineering Department, University of California-Los Angeles, Los Angeles, CA 90095*
[b] *Stanford Synchrotron Radiation Lightsource, SLAC National Accelerator Laboratory, Menlo Park, CA 94025*
[c] *Beijing Synchrotron Radiation Facility, Institute of High Energy Physics, Chinese Academy of Sciences, Beijing 100049, China*

**D. A. S.: E-mail: dasimonetti@ucla.edu.*
**Y. L.: E-mail: liuyijin@slac.stanford.edu.*
**S. R. B.: E-mail: srbare@slac.stanford.edu.*

Details of experimental methods, model derivations, and additional characterization results are available in the supporting information for this article via a link at the end of the document.

Herein, we report results from the use of synchrotron-based X-ray techniques to quantitatively elucidate how the fundamental kinetics relates to the evolution of chemical heterogeneity of two different copper oxide sorbent materials during reaction with hydrogen sulfide to form copper sulfide. X-ray absorption spectroscopy (XAS) tracked changes in the average chemical environment of Cu atoms during sulfidation, and allowed determination of CuO conversion with time, providing direct determination of the bulk sulfidation kinetics. These data were complemented using transmission X-ray microscopy (TXM) that probed individual micrometer sized CuO particles to quantify chemical and structural changes on a length scale of tens of nm. Our primary discoveries show that H_2S removal reaction kinetics exhibit similar trends in fixed bed reactors and in individual µm-sized particles. However, reaction fronts proceed through the diameter of the these particles heterogeneously. Furthermore, we quantitatively identify, for the first time, H_2S concentration gradients within particles as small as 10 µm, which indicate pore diffusion even at very small length scales. We also show that copper oxide sorbent samples with similar physical characteristics exhibit approximately 3 times different sulfidation conversion with reaction rate constants that differ by a factor of 1.5. We conclude that differences at the crystallite level must be taken into account with differences in pore structure and/or grain size of CuO even at tens of µm length scales to completely describe the observed differences in sulfidation reactivity. Furthermore, we suggest that the formation of different copper sulfide products also influence the capacity and rate differences between similar copper oxide materials. These results represent an advancement toward the fundamental molecular understanding of gas-solid reactions by simultaneously collecting kinetic data and characterizing the real-time chemical and structural changes of the solid phase.

Experimental

Materials

Copper (II) oxide particles were prepared by dropwise addition of aqueous 0.1 M sodium hydroxide solution (BDH, 97% minimum assay) to aqueous 0.1 M copper (II) nitrate trihydrate (Sigma Aldrich, 99.0%) solution under continuous mixing. The copper (II) hydroxide precipitate was then vacuum filtered and dried in air at 353 K for 14 hours. The precipitate was treated in air at 823 K (0.7 K min^{-1}) for 4 h. This sample is denoted as CuO-2. A commercially produced copper-based material (HiFUEL W230; lot number L04Y006; 63.5 wt% CuO, 25 wt% ZnO, and 10 wt% Al_2O_3) was purchased from Alfa Aesar. This sample is denoted as CuO-1.

Fixed bed experiments

Reactive adsorption of H_2S was studied in an apparatus with plug-flow hydrodynamics. Flow rates of gaseous H_2S and N_2 were introduced via mass flow controllers (MKS GE50A and GM50A). Feed to the reactors consisted of H_2S in N_2 (900-1000 ppm-vol) and was produced by diluting a 1.0% H_2S (Praxair UHP) in N_2 mixture with UHP N_2. Powder adsorbent samples (155-260 mg) were sieved (+200-100 US mesh; 75-125 µm agglomerate diameter) and fixed between plugs of quartz wool in a 0.25-inch outer diameter tubular, stainless steel reactor. All gas transfer lines and the interior of the reactor were treated with an inert coating (SilcoNert 2000) to mitigate H_2S adsorption onto tubing walls. Compositions of feed and effluents were determined using online gas chromatography (Agilent 7890B) with a sulfur chemiluminescence detector (SCD; Agilent 755) and continuous gas phase FTIR spectroscopy (MKS Multigas). Analysis of the intra-particle heat transfer criterion indicate the absence of intra-particle temperature gradients (see SI).

Non-synchrotron characterization techniques

Scanning Electron Microscopy (SEM) images of the CuO materials were taken before and after sulfidation using a Nova Nano 230 in the Materials Science and Engineering Department at UCLA. X-ray diffraction patterns were collected using a Panalytical X'pert Pro Powder X-Ray diffractometer, with a Cu-K_α source, in the UCLA Molecular Instrumentation Center. N_2 physisorption isotherms were collected at 77 K on a Micromeritics ASAP 2020 Plus. Prior to adsorption, the samples were treated at 423 K (10 K min^{-1}) under flowing N_2 for 8 h. Surface areas were calculated using the Brunauer–Emmett–Teller (BET) method, and pore volumes were calculated using the Barrett-Joyner-Halenda (BJH) method.

Synchrotron-based X-ray characterization

XAS and TXM measurements (shown schematically in Figure 1, collected at beamlines 2-2 and 6-2[15] at the Stanford Synchrotron Radiation Lightsource) were performed in order to establish a comprehensive understanding of the reaction kinetics. Bulk XAS data provide spectra with good signal to noise and are sensitive to subtle chemical changes in the chemical state of the copper atoms. However, bulk measurements miss the reaction front propagation within individual particles. Two- and three-dimensional X-ray spectro-microscopy, with spatial resolution down to 30 nm has the ability to map chemical variations across µm-sized particles[16-18] and can identify reaction fronts as they proceed through particles. In this work, we designed, constructed, and implemented two different gas phase reaction cells (Figures 1B and 1C) that are compatible with the experimental criteria of TXM and XAS, respectively.

Transmission X-ray images were collected using the full-field TXM at beam line 6-2 of the Stanford Synchrotron Radiation Lightsource, SSRL. The X-rays from a 56 pole 0.9 Tesla wiggler pass through several mirrors and are then focused to a spot size of a few hundred micrometers, which acts as the virtual source for the microscope. The monochromator installed at beam line 6-2 is a liquid nitrogen cooled double-Si(111) crystal system. The monochromator selects a narrow band pass from the incident X-ray, providing quasi-monochromatic illumination over a 2.1– 17.0 keV range for the optics downstream. A mirror pitch feedback system is installed to monitor the micrometer-level beam movements and adjust the toroidal mirror for stabilizing the beam. The TXM, designed to work over an energy range of ~5–14 keV, utilizes a capillary condenser to focus the beam to a spot with size down to a few tens of micrometers. A Fresnel zone plate with 200-µm diameter and 30-nm outermost zone width is employed to achieve a magnification of around 50 (depending on the energy configuration of the incident X-rays), which is further increased by a factor of 10 using the optical objective lens downstream of the scintillator crystal. A 2048 by 2048 pixel CCD optically coupled with the scintillator crystal is used to collect the projection images. The nominal spatial resolution of this system is ≈30 nm confirmed by a Siemens calibration standard and modulation transfer function.

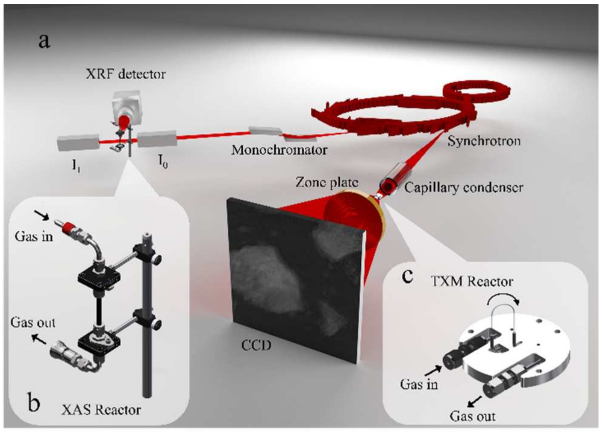

Figure 1: a) Schematic of experimental setup for sulfidation of CuO samples at the XAS and TXM beam lines. b) XAS cell schematic used for the room temperature sulfidation of CuO. c) TXM cell schematic featuring 0.1 mm quartz capillary used for the room temperature sulfidation of CuO.

In our experiments, the energy scan was coupled with the full-field imaging. Transmission images were recorded at over 100 energy points. Over the near edge region, an energy step of 1 eV was chosen to achieve the necessary energy resolution for X-ray absorption near edge structure (XANES) analysis. The energy step outside of the near edge region was 10 eV, covering a relatively large energy window for proper normalization or the spectra. The reduction of the spectro-microscopic data is performed using an in-house developed software package known as TXM-Wizard[15].

For *in-situ* TXM measurements, copper oxide samples were ground into a fine powder. Less than 1 mg of the sample was loaded into a 0.1 mm OD quartz capillary with a 0.01 mm wall thickness that had been previously heat treated into a U shape. X-ray imaging was conducted around the Cu K-edge (~8979 eV), which is sufficient to penetrate through the capillary cell and sample. Both ends of the capillary were cut off to create a U-shaped tube. The U-shaped capillary was glued into a base plate (see SI for drawings) using 5-minute epoxy. The gas delivery system at beamline 6-2 of SSRL allowed for delivery of different gas environments.

Cu K-edge, 8979 eV, XAS spectra were collected in transmission mode on the bending magnet beamline 2-2 at SSRL. The incident beam energy was selected using a water-cooled Si (220) phi = 0 monochromator with a beam size of 1 mm vertically x 3 mm horizontally. The ion chambers were filled with nitrogen gas. XANES scans were collected every 7 minutes. Extended X-ray absorption fine structure, EXAFS, scans were collected every 15 minutes. A copper foil was scanned simultaneously for energy calibration.

For *in-situ* XAS experiments, copper oxide samples were ground into a fine powder. Approximately 12 mg of CuO-1 was diluted with 48 mg of boron nitride (Sigma Aldrich) to achieve between 2-3 absorption lengths given the geometry of the experimental cell. In a similar manner, 10 mg of CuO-2 was diluted 100 mg of γ-alumina and 100 mg boron nitride to give a similar absorption length. The addition of the γ-alumina in the copper oxide nanoparticle sample was to prevent the sample bed from packing under gas flow. Approximately 50 mg of each sample was packed into a 10 cm long 6 mm OD glassy carbon tube (HTW Hochtemperatur-Werkstoffe GmbH) and stabilized with glass wool to prevent sample movement under gas flow. The glassy carbon tube was mounted into a flow through cell that acts as a plug flow reactor. The cell was purged with flowing helium prior to data collection.

Gases used during the in-situ XAS and TXM sulfidation experiments were helium (99.95%, Airgas) and 1000 ppm H_2S in helium (Airgas).The gas flow rates and pressures for the XAS and TXM measurements were 10 mL(STP)/min and 1 atm, and 2 mL(STP)/min and 1 atm, respectively. Samples were exposed to flowing helium while spectra, EXAFS and energy-resolved TXM images, were collected to determine the initial state of the copper in each sample. Maintaining the same flowrates as above, the helium was replaced with the 1000 ppm H_2S/He blend while XANES scans or energy resolved TXM images were collected. The copper oxide samples were exposed to sulfidation conditions for approximately 10 hours during the *in-situ* XAS and TXM measurements. The samples were purged with flowing helium at the end of the sulfidation process.

Results and Discussion

Chemical and physical characteristics of CuO samples

Both CuO samples were characterized to identify their initial chemical composition, crystalline phases, and pore structure (see SI for details). Diffraction patterns for the two samples show only characteristic peaks for hexagonal CuO. Analysis of the peak at 2θ = 37°, CuO (1 1 1), indicates that the CuO exists as crystallites of 28.3 nm and 2.8 nm in CuO-2 and CuO-1, respectively. No characteristic ZnO peaks were observed for CuO-1, suggesting that the zinc oxide is either amorphous or has crystallites below the detection limit of XRD. SEM images reveal particles that are 1-5 µm in diameter consisting of agglomerates of smaller (<1 µm) particles (CuO-2) and 5-15 µm sized particles, also consisting of agglomerates of smaller (~1 µm) particles (CuO-1) (see SI). The best-fit model of the Cu K-edge EXAFS data characterizing both CuO-1 and CuO-2 contained only scattering paths matching hexagonal CuO (see Table S6 in the SI). The coordination numbers for all paths are lower than those of bulk CuO, and are smaller for CuO-1 than

CuO-2, consistent with the XRD that the CuO-1 contains smaller CuO crystallites than CuO-2. We note that there were no detectable scattering paths from Cu-Zn or Cu-Al contributions in CuO-1. However, while the Cu K-edge XANES spectrum of CuO-2 contains spectral features that match those of monoclinic CuO (see SI), the XANES of CuO-1 appear to be slightly modified. This may be a result of the small crystallite size[19] or from an interaction of the CuO with the ZnO or Al_2O_3 as observed in other mixed oxide samples[20,21]. Analysis of the pore structures of these materials from N_2 physisorption data (see Table S1 in SI) reveal that CuO-2 has 23% more total pore volume (0.17 $cm^3\ g^{-1}$) than to CuO-1 (0.14 $cm^3\ g^{-1}$), with BET surface areas of the two samples being similar (63 $m^2\ g^{-1}$ and 59 $m^2\ g^{-1}$ for CuO-1 and CuO-2, respecitvely). The pore size distrubutions for the unreacted copper oxide samples (Figure 2) show that a majority (65% and 71% for CuO-1 and CuO-2, respecitvely) of the total pore volumes of both samples is contained within pores of greater than 30 nm diameter. CuO-2 exhibts 35% more total pore volume than CuO-1 within pores greater than 30 nm diameter, and CuO-2 has a peak in the pore size distribution at ~132 nm pore diameter whereas CuO-1 exhibits a monotonically increasing distribution from 30-250 nm. In summary, the characterization data indicate that the copper oxide phases of the two samples studied herein consist of crystalline CuO with a majority of pore volume contained in pores of 30-200 nm diameter. The most substantial measurable difference are the CuO crystallite size and the particle agglomerate size, and the pore size distribution.

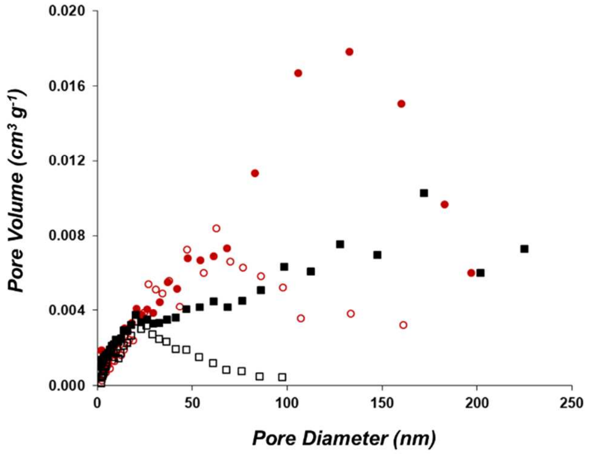

Figure 2: Pore size distributions for CuO-1 (black squares) and CuO-2 (red circles) before (filled symbols) and after (open symbols) reaction with 1000 ppm H_2S at ambient temperature and pressure in a fixed bed reactor.

Fixed bed sorption experiments

The sulfidation kinetics of the two samples (at ambient temperature and pressure) were measured in fixed bed sorption experiments to determine the saturation capacities and sorption rate parameters from the breakthrough curves (Figure 3). In these breakthrough curves, the time on stream is normalized against the weight-hourly space velocity (mass flowrate of H_2S divided mass of adsorbent). This normalization procedure accounts for any small variation in inlet H_2S flowrate and adsorbent bed size and allows for the direct comparison of breakthrough curves.

The breakthrough data for CuO-1 (Figure 3, red) and CuO-2 (Figure 3, blue) both exhibit a sickle shape which can be modeled using a linear driving force equation for the rate of H_2S adsorption[4,5] (Equations S4-S6 in the SI; Figure 3, black). CuO-1 exhibited a higher H_2S capacity (12 ± 0.7 wt%; 44% conversion) compared to CuO-2 (6.0 ± 0.2 wt%; 14% conversion). The total resistance to H_2S uptake (see Equation S7in SI) was determined from linear least square regression of the data (see Table S2 in SI). The resistance from bulk and pore diffusion (see Equation S7 and Table S2) were calculated from known engineering correlations (Equations S8-S10 in SI). The calculated values for bulk diffusion (22,000 s^{-1} and 7400 s^{-1} for CuO-1 and CuO-2, respectively) and pore diffusion (260 s^{-1} and 90 s^{-1} for CuO-1 and CuO-2, respectively) mass transfer coefficients are more than an order of magnitude larger than the total experimentally derived resistance to H_2S uptake for each sample. Thus, bulk and pore diffusion resistances have negligible impact on the measured rate of H_2S removal under these experimental conditions, and the experimentally determined reaction rate parameters reflect only phenomena that occur at the molecular scale (i.e, chemical reaction at the surface and/or solid state diffusion through product layers to reaction interfaces). The linear driving force rate parameters were derived from the total uptake resistance according to Equation S7 in the SI. The reaction rate parameter was a factor of 10 larger for CuO-2 ($4.3 \pm 0.2 \times 10^{-4}\ s^{-1}$) than for CuO-1 ($4.0 \pm 0.3 \times 10^{-5}\ s^{-1}$).

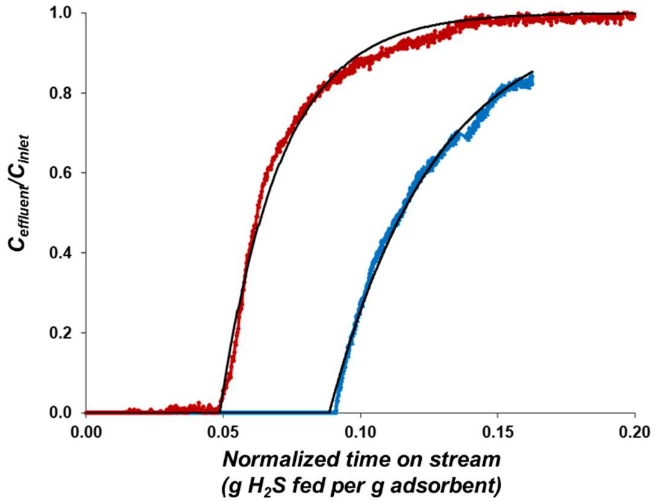

Figure 3: Normalized concentration-time profiles for reaction of CuO-1 (red) and CuO-2 (blue) with 1000 ppm H_2S at ambient temperature and pressure in a fixed bed reactor. Normalized time is calculated by multiplying the time on stream by the mass flowrate of H_2S and dividing by the mass of adsorbent. Solid lines are model fits to the data[4,5].

Analysis of copper oxide samples after reaction reveal a loss of total pore volume within pore diameters of 70-200 nm in both samples (Figure2 and Table S1 in SI). The loss in pore volume occurs to a greater extent within CuO-1 (0.14 to 0.051 cm^3 g^{-1}) compared to CuO-2 (0.17 to 0.11 cm^3 g^{-1}). A higher extent of pore volume loss for CuO-1 compared to CuO-2 is expected because CuO-1 exhibited higher conversion than CuO-2 and because a volume expansion occurs upon formation of CuS (density of 4.6 g cm^{-3}) from CuO (density of 6.6 g cm^{-3}). However, the higher rate parameter exhibited by CuO-2 (compared to CuO-1) suggest that the faster formation of CuS in sample CuO-2 results in morphology changes (i.e., covered CuO surfaces or rapid pore loss at the surface regions of particles) that impede access of H_2S to the CuO interface and that lead to lower conversion.

Sulfidation kinetics from bulk XAS measurements

Direct determination of the bulk sulfidation kinetics of CuO-1 and CuO-2 were determined using *in-situ* XAS. The Cu K-edge spectra show changes concomitant with a change from CuO-like features to those of CuS. Linear combination fitting (LCF) of the spectra was used to determine the extent of CuO conversion as a function of reaction time (Figure 4). Conversion rapidly increases with time for both samples during the first 10-30 minutes with a rapid decrease in rate thereafter.

After ≈10 h time on stream, the reaction appears to stop (conversion approaches a constant value with increasing time). The initial region lasted 3 times longer for CuO-1 (30 min) then CuO-2 (10 min), and the total conversion to CuS was ~3-fold higher for CuO-1 than CuO-2 (38% vs 13%), similar to the results of the fixed bed experiments. The LCF XANES data (Figure 4) data were analyzed using the random pore model[10] (RPM). The RPM separates the conversion versus time data into a reaction rate controlled regime and a diffusion controlled regime as conversion increases (see SI), and values for the reaction rate constants and effective diffusivities were regressed from the data. The rate constant for CuO-2 ($8.4 \pm 2.6 \times 10^{-3}$ cm^4 mol^{-1} s^{-1}) was higher than that for CuO-1 ($5.6 \pm 0.9 \times 10^{-3}$ cm^4 mol^{-1} s^{-1}), indicating that rapid reaction rates lead to morphological changes that could restrict transport of H_2S and ultimately to the early onset of slower, diffusion controlled reactions. The effective diffusivity in the diffusion-controlled regime was higher for CuO-2 than CuO-1 ($2.0 \pm 0.2 \times 10^{-12}$ vs $1.1 \pm 0.1 \times 10^{-12}$ cm^2 s^{-1}) suggesting that restriction of H_2S to CuO surfaces is more severe in CuO-1 than CuO-2 during their respective diffusion controlled reaction regimes because of higher product content within CuO-1 than CuO-2. While the access to reactive surfaces is apparently more facile in CuO-2 (than CuO-1) during the diffusion-controlled regime, the much earlier onset of this regime mitigates this apparent advantage. Indeed, these data reveal that slower reaction rates are beneficial to extending reaction controlled sorption rates to achieve higher conversions.

Previous studies on H_2S reactions with ZnO and ZnO doped with Cu or Ni[6-9] attributed improvements in reaction rate and conversion to dopants (e.g., Cu) that can facilitate the oxidation of the sulfur in an adsorbed HS^- species from S^{2-} to S^-. When Cu is the dopant in ZnO, this more facile oxidation step occurs because Cu is more easily reduced than Zn. This oxidation of S leads to a lower energy barrier for H-S dissociation with the final reaction steps being re-reduction of S^- to S^{2-} (with oxidation of Cu^+ to Cu^{2+}) and formation of ZnS[6,7]. Thus, conversely, the presence of Zn (even in small amounts) within CuO may inhibit HS-S bond dissociation on CuO leading to the lower observed sulfidation rate parameters on CuO-1 compared to CuO-2. Slower sulfidation reactions may prevent rapid coverage of the reactive CuO surface, allowing access to H_2S molecules and leading to the higher observed conversions on CuO-1 compared to CuO-2.

However, the characterization data presented previously indicate that both samples in this study are comprised of crystalline CuO, and there is no conclusive evidence for significant interaction between the Zn and Cu at the atomic scale (as evidenced by the EXAFS modeling data presented previously and shown in Table S4) for CuO-1. In addition, both samples have similar initial total pore volume and surface area (see SI). Furthermore, while the shapes of the pore size distributions are different, both materials contain a majority of their total pore volume distributed across pores with similar diameters. In fact, materials with higher total pore volume distributed within pores of wider diameter (as is the case with CuO-2 compared to CuO-1) are expected to exhibit higher conversion because they have more volume to accommodate the volume expansion that occurs upon conversion of CuO to CuS[10,11]. Therefore, the differences in reaction rate constant and final conversion in our study are unexpected and likely result from differences in the initial copper oxide surface (e.g., preferentially exposed planes and/or defects that result from the differences in crystallite sizes).

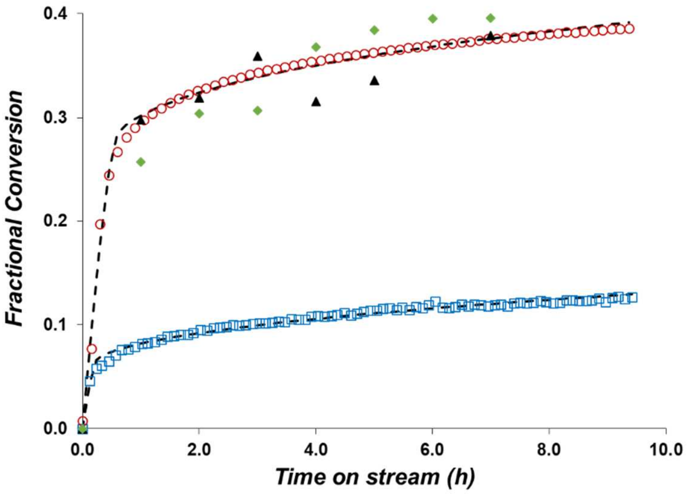

Figure 4: Fractional conversion of CuO to CuS as a function of time determined by the LCF of XAS experiments for fixed beds of CuO-1 (red circles) and CuO-2 (blue squares) and for individual particles of CuO-1 imaged by TXM spectro-

microscopy. Black triangles represent conversion of the 10 µm particle in Figure 5A, and green diamonds represent the 16 µm particle in Figure 5A. Black lines are RPM fits. Standard errors are ±0.2% of the conversion value.

Furthermore, on predominantly Zn-based materials, the final redox step (S^- to S^{2-}) is likely to occur for all H_2S molecules converted because ZnS is the only product that can form with Zn^{2+}. In contrast, a variety of copper sulfide products can form (Cu_xS_y with $1 \leq x/y \leq 2$) because of the multiple oxidation states of Cu and S (S^{2-} and $(S^-)_2$). Thus, we also propose that the differences in the reaction rate constants (and in the conversions) measured in this work may also result from differences in the specific Cu_xS_y product stoichiometry which could impact the evolution of the reactant-product interface. Furthermore, the formation of different (or multiple) Cu_xS_y products suggest that the single reaction assumption (i.e., formation of only CuS) for both materials is insufficient. Therefore, additional studies are necessary to characterize sulfide products and to construct a more detailed atomistic-level mechanism that includes the formation of all relevant copper sulfide products.

Sulfidation kinetics of individual particles via TXM

As mentioned previously, both porosity and chemical structure influence the average rate of reaction in particles of metal oxides[8-11]. Thus, heterogeneity at the particle or sub-particle scale can critically affect the performance of the solid phase, and it is of fundamental interest and practical importance to visualize the evolution of this chemical heterogeneity at fine length scales. Thus, we performed 2-dimensional XANES mapping on particles of the CuO samples (using TXM). Figure 5A shows chemical maps, determined by LCF, of a 10 µm and a 16 µm particle of CuO-1 during the course of exposure to 1000 ppm H_2S for 8 hours. Direct observation of the chemical maps in Figure 5A suggests that the evolution of the chemical heterogeneity follows a complex pathway, highlighting the importance of studying the particles using a chemically sensitive probe with good spatial resolution.

For quantification of the XANES imaging data, we first average the chemical signatures of the entire 10 µm particle and the common areas in the 16 µm particle, respectively. The amounts of remaining CuO in both particles change over time and, follow the same trend as the data from the bulk XAS measurement (Figure 4). The matching trends of both the bulk XAS and averaged TXM XANES results not only confirm the reliability of our measurements but also suggest that a critical length scale of the chemical heterogeneity is at the sub-single particle level. For a better visualization of the dynamic evolution of the chemical distribution at sub-particle level, we segmented the reaction front based on the local chemical composition of the 10 µm particle. The pixels associated with local CuO/CuS ratio at 1:1 (indicating 50% conversion of CuO to CuS) are labeled in white in Figure 5B and are defined as the reaction front. The sulfidation front clearly initiates within the outer portions of the particle (at distances that are >90% of the radius) and propagates towards the center of the particle after being exposed to the H_2S stream for ~5-6 hours. The morphology of the reaction front also changes from isolated pockets into a complex interconnected network upon progression of the reaction. At the beginning of the reaction, the nucleation events dominate the system leading to relatively fast conversion of CuO to CuS (see Figure 4). After the first few hours, the propagation of reaction front in the solid phase becomes the dominating event and the system becomes diffusion limited, slowing down the overall conversion efficiency.

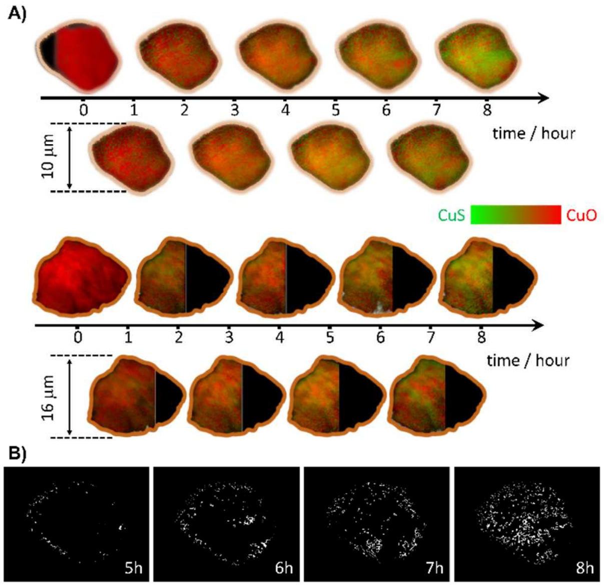

Figure 5: A) *In-situ* Chemical maps of CuO particles during sulfidation reaction. B) Development of the reaction front (defined by the voxels with a chemical composition of 50% CuO and 50% CuS)

Analysis of the entire volume of both particles reveals similar kinetics as those measured in a reactor containing multiple particles, indicating that analysis of reaction of mg amounts of powders can produce kinetic expressions suitable for reactor scale design and operation. However, the different dynamic conversion profiles measured at different radial positions within individual particle indicates that H_2S concentration gradients (and thus, pore diffusion) exist even at very small length scales and cannot be detected by analyzing the kinetics in fixed beds of particles. The conversion versus time data at various radial positions within the 10 µm particle (Figure 6) were analyzed using the RPM to quantitatively determine any kinetic differences with radial position. The RPM predicted the conversion versus time data with good agreement to the experiment data (Figure 6A). However, the rate parameters (see SI Table S5 for 95% confidence intervals) exhibited a sharp decrease at positions less than 90% of the radius (Figure 6B).

Furthermore, the diffusivity exhibited a linearly increasing trend with radial distance into the particle (Figure 6B). These conversion profiles measured from TXM suggest that H_2S concentrations are higher within the outer regions of the particle, leading to higher initial reaction rates, faster buildup of product layers, and more rapid pore structure change. Conversely, lower concentrations within the particle interior would lead to slower reaction that allows diffusion to occur more rapidly as product layers form more slowly. This explanation is supported by the increasing values of the effective diffusivity with increasing proximity to the particle interior. Furthermore, the abrupt decrease in reaction rate constant (followed by a more gradual decrease of the reaction rate constant) indicates that this value is dependent upon H_2S concentration. Thus, this reaction rate constant is an apparent rate constant and not an intrinsic rate constant as has been suggested by previous work[10,11]. This conclusion further supports the need for identification of fundamental mechanism for the reaction between CuO and H_2S that can describe this reaction across a wide range of conditions.

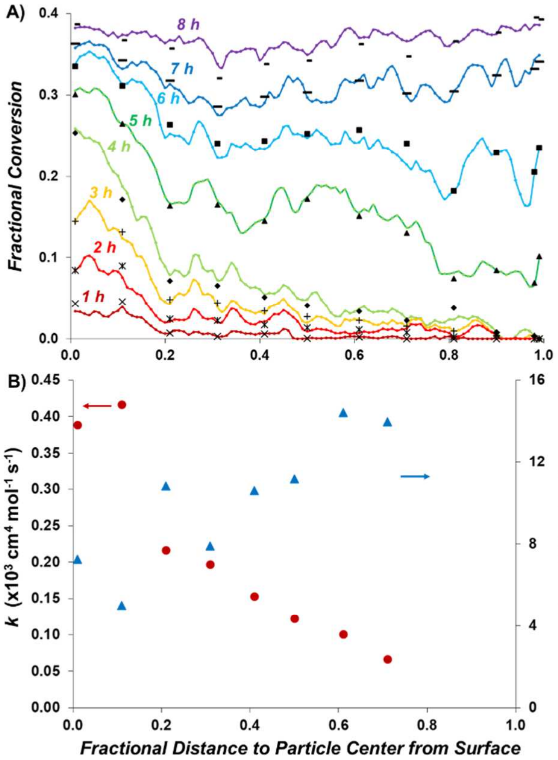

Figure 6: A) Fractional conversion (lines are data; symbols are model predictions) of CuO to CuS at various radial distances and at various times on stream within the 10 µm particle in Figure 5A. The value of zero is the particle surface and the value of 1 is the particle center. Standard errors are ±0.2% of the conversion value. B) RPM rate constants (k) and effective diffusivities (D_e) determined from the time dependent conversion data at various radial positions.

In conclusion, the observations from the *in-situ* XAS and TXM are consistent with the conventional kinetic studies that evaluate the role of the porosity and chemical structure in affecting the bulk performance of CuO for H_2S removal. These phenomena were quantitatively probed via TXM of individual particles to show that average kinetics within single particles mirror the reaction kinetics measured from fixed bed of sorbents. Similarly, analysis of data from XAS of a gradientless reactor reveals the same kinetic differences between the two CuO samples as analysis of breakthrough curves in a fixed bed experiment with sharp axial concentration gradients. However, the growth of reaction fronts proceed heterogeneously within solid phase particles and pore diffusion persists even for particles less than 10 µm in size. This combined characterization-kinetic analysis ultimately revealed that chemically and structurally similar CuO can exhibit different kinetics upon reaction with H_2S and that explaining these differences must include more detailed reaction stoichiometry and analysis of specific surface properties of the reactant and product phases.

Conflicts of interest

There are no conflicts to declare.

Acknowledgements

Acknowledgement is made to the Department of Chemical and Biomolecular Engineering and the Office of Equity, Diversity, and Inclusion at UCLA and to the donors of The American Chemical Society Petroleum Research Fund for partial support of this research. Use of the SSRL, SLAC National Accelerator Laboratory, is supported by the U.S. Department of Energy, Office of Science, Office of Basic Energy Sciences under Contract No. DE-AC02-76SF00515. K. Z. acknowledges the National Key Research and Development Program of China (Grant No. 2016YFA0400900) and the National Natural Science Foundation of China (Grant No. 11535015, U1632110) for partial support of this research.

Notes and references

1 A. I. Olivos-Suarez, A. E. Szecsenyi, J. M. Hensen, J. Ruiz-Martinez, E. A. Pidko and J. Gascon, *ACS Catal.*, 2016, **6**, 2965-2981.
2 A. J. Hidnay, W. H. Parrish, Fundamentals of Natural Gas Processing. CRC Press: Boca Raton, 2006.
3 C. Song, X. Ma, *Appl. Catal. B: Enviorn.* 2003, **41**, 207-238.
4 S. R. Dunne, Industrial Gas Separation Processes. In Zeolites in Industrial Separation and Catalysis, Kulprathipanja, S., Ed. Wiley-VCH: Weinheim, Germany, 2010; pp 273-304.
5 D. M. Ruthven, Principles of Adsorption and Adsorption Processes. Wiley-Interscience: 1984
6 A. Samokhvalov, B. J. Tatarchuck, *Catal. Rev. Sci. Eng.* 2010, **52**, 381-401.
7 A. Samokhvalov, B. Tatarchuck, *Phys. Chem. Chem. Phys.* 2011, **13**, 3197-3209.
8 J. B. Gibson, D. P. Harrison, *Ind. Eng. Chem. Proc. Des. Dev.* 1980, **19**, 231-237.
9 S. Lew, A. F. Sarofim, M. Flytzani-Stephanopoulos, *Ind. Eng. Chem. Res.* 1992, **31**, 1890-1899.
10 S. K. Bhatia, D. D. Perlmutter, *AIChE J.* 1980, **26**, 379-386.
11 P. A. Ramachandran, L. K. Doraiswamy, *AIChE J.* 1982, **28**, 881-900.
12 J. Ruiz-Martinez, A. M. Beale, U. Deka, M. G. O'Brien, P. D. Quinn, J. F. W. Mosselmans, B. M. Weckhuysen, *Angew. Chem. Int. Ed.* 2013, **52**, 5983-5987.
13 M. Flytzani-Stephanopoulos, M. Sakbodin, Z. Wang, *Science.* 2006, **312**, 1508-1510.

14 L. Neveux, D. Chiche, J. Perez-Pellitero, L. Favergeon, A. S. Gay, M. Pijolat, *Phys. Chem. Chem. Phys.* 2013, **15**, 1532-1545.
15 Y. Liu, F. Meirer, P. A. Williams, J. Wang, J. C. Andrews, P. Pianetta, J. *Synchrotron Rad.* 2012, **19**, 281–287.
16 J. Je. Kim, M. Kaviany, S. Y. Son, M. Kim, *J. Synchrotron Rad.* 2011, **18**, 773-781.
17 I. D. Gonzalez-Jimenez, *Angew. Chem. Int.* 2012, **51**, 11986-11990.
18 F. Lin, *Chem. Rev.* 2017, **117**, 13123–13186.
19 A. Kuzmin, J. Chaboy, *IUCrJ.* 2014, **1**, 571-589.
20 S. Velu, K. Suzuki, C. S. Gopinath, H. Yoshida, T. Hattori, *Phys. Chem. Chem. Phys.* 2002, **4**, 1990-1999.
H. Liu, F. Zeng, S. Gao, G. Wang, C. Gong, F. Pan, *Phys. Chem. Chem. Phys.* 2013, **15**, 13153-13161.

TOC GRAPHIC

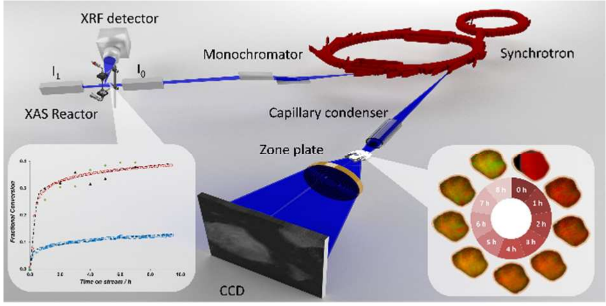

In-situ spectroscopic techniques provide kinetic and chemical structure data for elucidation of reaction mechanisms and pathways during reactive separations.